Nanoscale

Accepted Manuscript

This article can be cited before page numbers have been issued, to do this please use: J. Kim, H. Eguchi and Y. Ishikawa, *Nanoscale*, 2017, DOI: 10.1039/C7NR02229H.

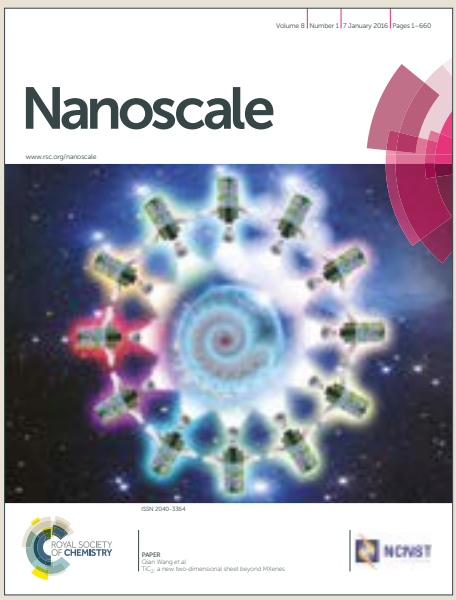

ROYAL SOCIETY OF CHEMISTRY

rsc.li/nanoscale

View Article Online
DOI: 10.1039/C7NR02229H

Anticancer luminescent gold quantum clusters for *in situ* cancer-selective marking-imaging-targeting

Jeong-Hwan Kim,[1]* Haruki Eguchi,[2] and Yoshihiro Ishikawa[1]

[1]Cardiovascular Research Institute, Yokohama City University, Graduate School of Medicine, Yokohama, 236-0004, Japan.
[2]Advanced Applied Science Department, Research Laboratory, IHI Corporation, Yokohama, 235-8501, Japan.

*Corresponding author. Email: jeongkim@yokohama-cu.ac.jp

Abstract

Ultrafine Au quantum clusters (QCs) are synthesized by etching host Au nanoparticles in the presence of ethylenediamine (en), exhibiting both high photoluminescence (PL) and specific anticancer activity. The cutting-edge of such QC compound involves subnanometer size of a rhombohedral Au_8, consisting with 8 units of anticancer motif Au^+(en) complexes (Au(en)QCs), which attribute to photo- and physico-chemical stability as well as subcellular theranostic activity in intracellular PL-imaging and targeting *in situ*. Moreover, the Au(en)QCs can be surface-encapsulated by transferrins (Tf), creating Tf-Au(en)QCs, as a multipurpose drug carrier due to numerous merits that include cancer-selective biolabeling, high loading/release efficiency, high activity against drug-resistant tumor cells, low toxicity on normal cells, and physiological stability against biothiols, e.g., glutathiones. These versatile features due to the intrinsic optical and anticancer property would be potential as a single-drug delivery PL-probe for pre-clinical applications, which yet been realized using conventional nanoclusters.

View Article Online
DOI: 10.1039/C7NR02229H

1. Introduction

Ligand reactivity at metal interface plays critical roles in transition of bulk metals undoubtedly into unique nanomaterials with size-dependent properties, and bestows them with explicit atomic packing and functionalization. With the advance of ligand-engineered synthetic techniques, ultrasmall Au nanoclusters (NCs) with a diameter of less than 2 nm arranged in confined geometric structures are being emerged as a new class of optical probe material that has been extensively investigated in recent years.[1-11] Because these NCs differentiates them from bulk gold, gold nanocrystals, and gold complexes, by exhibiting unique quantum size effect in the “molecule-like” discrete electronic arrangement of the core together with extremely high surface-to-volume ratio. Thus, it is in charge for facilitating the applications in bio-imaging,[1-3, 7-12] bio-sensing,[1-3, 9-15] and catalysis,[1-3, 12, 16-18]

Normally, few-atom fluorescent AuNCs (Au_n, n=2~30) have been prepared by “bottom-up” template-based (polymers, DNA, and proteins) or ligand-protected (thiolate- or phosphine-capped AuNCs) techniques.[1-11] On the other hand, many AuNCs involves a “top-down” etching step in which excess thiolated ligands transforms larger nanoparticles (NPs) into smaller and more thermodynamically stable ones, exhibiting well-defined super-atomic structure with a countable “magic” number of Au atoms and discrete transited “molecule-like” electronic or photofluorescence (PL) behavior,[1-3, 18-21] Chen and his collaborators employed DNA, peptides, and amino acids to generate atomically precise Au_8NCs where they implemented biomolecule-induced etching of larger NPs or nanorods.[20] Recently, radical initators such as O_2 was used for efficient etching of gold by thiolates.[21] However, the detailed mechanisms of PL-origin have not

View Article Online
DOI: 10.1039/C7NR02229H

yet been clearly elucidated and most of the reported AuNCs have exhibited relatively low quantum yields (QY) and low stability over intercellular interferences, i.e., Au-interaction with serum albumins, enzymes, and biothiols, e.g., glutathione (GSH), which preclude their realistic function as PL-biotags.[11, 14, 18] Consequently, seminal work has presented that the size of these clusters can be quantitatively controlled with atomic precision,[1-3, 23-25] which this control gives access to tuning the optical and electronic properties prospects to realize high PL efficiencies. However, gaining precise structural and dynamical information on the ligand poses a major challenge, because the nature of the organic/metal interface is often vague visualization of possible distinct ligand conformations of the ligated NCs.

There is an urgent need for new first-in-class anticancer drug candidates to maximize effectiveness and selectivity of targeting tumor cells and to minimize side effects and drug resistance. The use of dual functions, both imaging and anticancer-activity, is an ideal way to boost the targeting efficacy of cancer therapy while significantly limiting the received dose and the possible damage to normal tissues. In this regard, most of reported AuNCs are cytotoxically inert due to the oxidation state is Au^0, which is only useful for biosafe labeling/imaging application. On the contrary, significant advances in valenced Au-based drug agents has been attained by utilizing Au^+, Au^{3+}, and their coordination ligand complexes as anticancer drugs,[26,27] revealing favorable cytotoxic specificity in generic cancer and drug-resistance cancer cells for some Au complexes over cisplatin,[28] though they do not have PL properties. To the best of our knowledge, there is no study in the development of organometallic-based AuNCs,

View Article Online
DOI: 10.1039/C7NR02229H

which shows both fluorescence and tumor-selective activity, to provide multipurpose platforms for rational single-drug delivery strategies in a minimally-invasive fashion.

Here, we demonstrate novel pathway for a simple, rapid, and effective preparation of highly fluorescent anticancer-active Au quantum clusters (QCs) at 25 °C, through etching host AuNPs by a petite bidentate amino-ligand, ethylenediamine (henceforth "en"), followed by a surface stabilization into metal transfer proteins, e.g., transferrins (Tf) in the presence of Na_2CO_3 (**Fig. 1**).

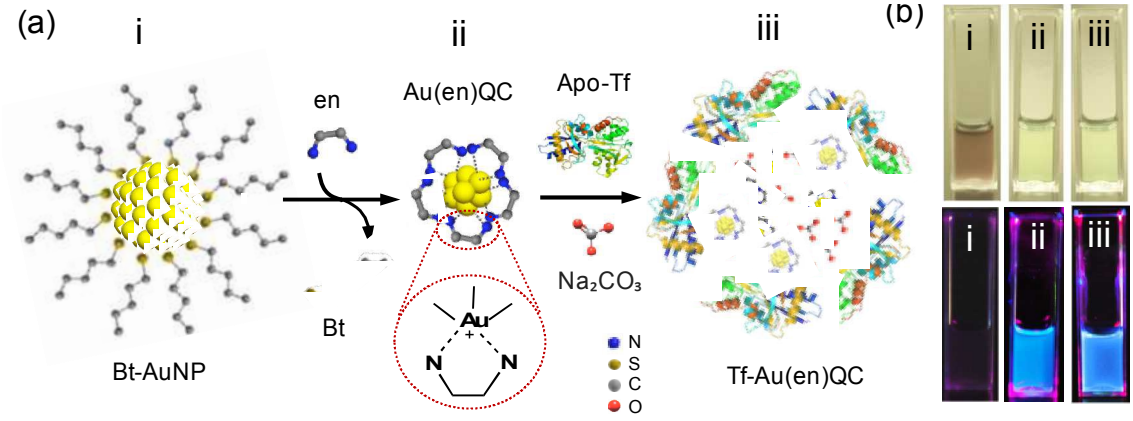

Fig. 1 (a) Schematic synthesis of Au(en)QCs and its Tf-encapsulation. Bt-AuNPs in DCM (i), ethylenediamine (en), 25 °C, 24 h, (ii) Au(en)QCs (showing an Au(en) complex-motif), (iii) Tf-encapsulated Au(en)QCs via Na_2CO_3. (b) Photos of Bt-AuNP (i), AuQC (ii), and Tf-Au(en)QC (iii) dispersions, in white light (the top) and UV light (365 nm) (the bottom).

2. Experimental section

2.1. General procedures

View Article Online
DOI: 10.1039/C7NR02229H

All water used was purified with an EASYpure® RF system (Barnstead, Dubuque, IA; 18.2 Ω). All solvents and reagents (ACS grade) including dichloromethane (DCM), ethylenediamine (en), sodium carbonate, and human serum apo-Tf were obtained from Sigma-Aldrich (Saint Louis, MO, USA). The gold salt, $HAuCl_4$, and butanethiol were obtained from Strem Chemicals (Newburyport, MA, USA) and Sciencelab.com, Inc. (Houston, TX, USA), respectively. The ~2.5 nm butanethiol (Bt)-stabilized gold nanocrystals were synthesized according to the modified Brust-Shiffrin method under a purified nitrogen atmosphere.[29]

2.2. Synthesis of ethylenediamine (en)-induced fluorescent AuQCs

The noble synthesis of Au(en)QCs was carried out via an etching reaction of preformed Bt-AuNPs in the presence of en ligands. Briefly, 1 mM of en was added in a test tube, containing 2 mg of Bt-AuNPs in 4 mL of dichloromethane (DCM). The reaction mixture was incubated at room temperature for 24 h with a gentle stirring. After the reaction, the prior brown color of NPs in DCM solution was disappeared, which demonstrated that the AuNPs were completely etched. The vapor pressure caused during the reaction was carefully ventilated under ambient condition, followed by blowing off the remained organic solvent with N_2 gas. Then, the sample pellets were re-dispersed in 4 mL of ddH_2O solution, using by a brief sonication, while the undissolved white-colored outbound thiol ligands and excess host AuNPs were separated by a mild centrifugation at 5,000 rpm for 30 min. The collected bright green solution was filtered and mixed with 4 mL of DCM containing 0.1% TFA to discard excess en and adjusted pH to 7.4, followed by washing with 4 mL of fresh DCM 10 times, repeatedly. After blowing off the

View Article Online
DOI: 10.1039/C7NR02229H

solvent, the Au(en)QC products was sealed and stored in dark for later studies. Yield 86%, Elemental analysis was conducted by a Perkin Elmer 2400 analyzer (Waltham, MA, USA): Anal. Found % C 9.01, H 1.96 N, 9.65; Calc % C 8.36, H 1.05, N 9.74.

2.3. Encapsulation of Au(en)QCs with human transferrins

As-prepared Au(en)QCs (0.5 mg/mL) in saline solution (pH 7.4) were added to human serum apo-Tf solution (1 mg/mL) in the presence of 15 mM sodium carbonate (pH 7.4) and stirred for 3 h in order to sequester the QCs into the Tf proteins. Then, the green-colored Tf-Au(en)QC complexes were spin down by a centrifugation at 100,000 rpm for 60 min and collected, following by a washing three times using the centrifugation process to remove unbound Tf molecules and Au(en)QCs. The purified products were re-dispersed in saline solution (pH 7.4) and briefly sonicated. The products were sealed and stored in dark at 4 °C for later studies.

2.4. Quantitation of loading/release of en-AuQCs

The drug-loading efficiency (DLE) (%) was measured as ($M_{initial\ AuQCs} - M_{AuQCs\ in\ excess}$)x100/($M_{initial\ AuQCs}$) (mg/g). The loading/release activity of the Au(en)QC-loaded Tf complex was monitored by measuring the PL-emission at λ_{max} 475 nm. Each sample at pH 5-8 was centrifuged and its PL-absorbance of supernatant solution was used to quantify the amount of Au(en)QCs released toward the supernatant, according to a pre-determined calibration curve. All of the release profiles are shown in cumulative mode.

2.5. Synthesis of $[Au(en)Cl_2]Cl{\cdot}2H_2O$

View Article Online
DOI: 10.1039/C7NR02229H

As a comparative standard anticancer complex, $Au(en)Cl_2$ was prepared according to the literature.[30] Briefly, $HAuCl_4$ (0.548 mM) and en (0.55 mM) were reacted in absolute ethanol at 25 °C for 20 min. Pale yellow crystals of $Au(en)Cl_2$ formed slowly, followed by filtration, concentration, and drying steps. Yield 84%, elemental analysis: Anal. Found % C 6.11, H 3.01 N, 6.92; Calc % C 6.01, H 3.03, N 7.01.

2.6. Physico-chemical characterizations

The absorption spectra of AuQC products were obtained using a DU-800 ultraviolet/visible/near-infrared (UV/Vis/NIR) spectrophotometer (Beckman Coulter Inc., Fullerton, CA). The PL emission spectra were collected using a Hitachi F-4500 fluorescence spectrometer (Hitachi Ltd., Japan) controlled by PL solution software. The optical path length of a quartz fluorescence cell was 1.0 cm. The excitation and emission slits were all set for a 5.0 nm band-pass. The sample mixtures in square quartz cuvettes were excited at 375 nm, and the emission spectra were collected from 300 to 800 nm. The fluorescence intensity at 475 nm was used to evaluate the performances of the QCs. The background for the fluorescence spectrum was deionized water for the AuQC, and 0.05 M sulfuric acid for the reference compound measurements (neither solution displayed any noticeable fluorescence). The spectrum of the reference compound, quinine sulfate (QS), $(C_{20}H_{24}N_2O_2)_2 \cdot H_2SO_4 \cdot H_2O$, dissolved in 0.05 M sulfuric acid was recorded immediately after obtaining the QC spectra. The absorption spectrum of QS peaks at 349 nm and the excitation wavelength was chosen for the QY measurements for the QC solutions. The fluorescence QY was measured with an integral sphere (JASCO, ILF-533, ϕ=10 cm) mounted on the fluorescence

View Article Online
DOI: 10.1039/C7NR02229H

spectrometer (JASCO, FP-6600). Sample solution was placed in a quartz sample cell of 10 mm optical path. The measurement was conducted with a fixed excitation wavelength of each sample (QYQS=51%).

The structural characteristics of the Au(en)QCs were assessed using HRTEM and the compositional profiles probed by EDX spectroscopy using a Cs-corrected FEI Titan (HRTEM, FEI, Pleasanton, CA, US) operating at 300 kV. For HRTEM analyses, 1.5 μL of each sample solution was deposited onto a 300 mesh Formvar-coated copper grid. No staining was used to alleviate any possibility of artifacts. After dehydration, the samples were examined using HRTEM at 300 keV. However, the crystal lattice of Au is hardly observed in this TEM image of AuNCs in aqueous solution due to the small size (< 1 nm). The NC core dimension is barely identifiable because the image was captured immediately after exposure to avoid aggregation of particles due to high energy electron beams during the imaging. A multimode AFM (Bruker, CA, US) was used to obtain the AFM data in tapping mode.

To quantify the total amount of gold in the AuQC sample, MS analysis was performed. 5 μL of methanol solution of AuQCs was mixed with 95 μL of a matrix solution (10 mg sinapinic acid + 250 μL Acetonitrile + 750 μL TFA (0.1% in deionized water). Then, 1.5 μL of the mixed solution was dispensed onto the sample plate and dried at room temperature. After drying in ambient air, a positive mode mass spectrum of the Au(en)QCs were acquired using a MALDI-TOF MS (Shimadzu Corp., Kyoto, Japan), operated by a pulsed Nd:YAG laser (355 nm) in the linear configuration.

View Article Online
DOI: 10.1039/C7NR02229H

To quantify the valence state of gold in the AuQC sample, XPS analysis was performed by a Kratos Axis Ultra^{DLD} 39-306 photoelectron electron spectrometer equipped with a monochromated AlKα source operated at 300 W (Manchester, UK).

To evaluate the surface charge characteristics of AuQCs and Tf-AuQCs, a gel electrophoresis was performed. 2% agarose (Gibco BRL, #15510-027) gel was prepared by weight in 0.5X TBE buffer (Tris-Borate-EDTA Buffer, #T3913, Sigma-Aldrich). The solution was heated to around 90 °C and was then cast in a gel tray (Sub-Cell GT Agarose Gel Electrophoresis System, Biorad, USA). Samples were diluted with 1/2 volume 1X loading buffer containing 10% glycerol and then loaded into the appropriate well (10 µL each) located at center of the gel. Gel was run bi-directionally at 100 V (8.3 V/cm) for 20 min: The AuQC samples are toward the anode if negatively charged or toward the cathode if positively charged. Then, the gel was visualized over UV light using a digital camera (Bio-Rad Inc.).

A Zetasizer Nano ZSP (Malvern Instruments Ltd, Worcestershire, UK) was used for dynamic light scattering (DLS) and zeta potential analyses. A PBS solution (pH 7.0, 100 mM) was used to prepare the Au(en) QC and Tf-Au(en)QC for the measurements of their DLS and zeta potentials.

The fluorescence images of cell samples in the absence/presence of Au(en)QC samples were captured by a Zeiss LSM 510 confocal laser scanning microscope system through a 100/40 objective lens, and 488 nm lasers were used to excite the QCs at 37 °C.

For the pH- and thermo-stability measurements, the pHs of purified AuQC products were adjusted from 2 to 10 by adding different amount of 1 M HCl or 1 M KOH.

View Article Online
DOI: 10.1039/C7NR02229H

The PL spectra measurements were triplicated and normalized to evaluate ΔPL%. The samples treated at different pH levels were also monitored 6 months after. Investigation of the temperature-dependence of AuQCs' fluorescence was also carried out at the range of 25 to 98°C in a conventional thermal cycler in a PCR platform (Bio-Rad Inc.) to maintain the thermal uniformity.

2.7. Simulation of Au(en)QC structures

We performed all electron relativistic calculations with double numerical basis including polarization functions,[31,32] using the discrete variational method (DVM).[31] The generalized-gradient approximation (GGA) by Becke, Lee, Yang, and Parr (BLYP)[31] was employed to an exchange-correlation orbital energy function model, which depends on both the local electron charge density and the magnitude of its gradient. In order to obtain structure of Au_8 cluster with the en member rings, we optimized the structure by wave functions and eigenvalues. Firstly, we set molecular structure according to a chemical formula of Au_8 cluster with the en member rings. Secondly, we dynamically optimized the structures without any empirical parameters. The structural optimization method is the direct inversion in the iterative subspace.[31] By resolving Kohn Sham equation that can approximate Schrödinger equation, in which the energy of a molecular or bulk state can be expressed as a function of electron charge density,[31] we were able to obtain the physical and chemical properties through wave functions and eigenvalues.

2.8. Cell culture, cell viability assay, and cell labelling/imaging

View Article Online
DOI: 10.1039/C7NR02229H

The human ovarian carcinoma A2780 and A2780*cis* cell lines were attained from Sigma-Aldrich. Human ovarian epithelial cell line (SV40) was obtained from Applied Biological Materials (ABM) Inc (Richmond, BC, Canada). Human melanoma cancer and HeLa cell lines were purchased from American Type Culture Collection (ATCC, Manassas, VA). These cell lines (~10^4 cells) were seeded in RPMI-1640 with L-glutamine and phenol red medium containing 10% fetal bovine serum and 1% penicillin–streptomycin. The culture media was replaced with fresh media and cultured for a further 48 h. After dispensing 100

µL of cell suspension (~5x10^3 cells per well) in a 96-well plate, the plate was pre-incubated for 24 h in a 5% CO_2 incubator. The cell density was kept constant at ~4x10^4 cells per well in the whole study unless otherwise stated. Then, the cell wells were exposed to different concentrations of the AuQCs, Tf-AuQCs, Au(en)Cl_2, or cisplatin (0.2-50 µM) for 24 h at 37 °C. After treatment, each well was incubated with 0.5 mg/mL XTT reagent for 4 h at 37 °C. Consequently, the absorbance at 450 nm was measured with a Multiskan GO UV-Visible spectrophotometer. The viability of treated cell wells was obtained as a percentage of the viability of unexposed wells. For live cell labeling/imaging, the cells were seeded at an initial density of ~4x10^4 cells per well in a 12-well culture plate. After 24 h incubation, the cells were exposed to 20 µM AuQCs or Tf-AuQCs in culture media for 2 h at 37 °C in a 5% CO_2 incubator, and then washed twice with PBS (pH 7.0, 100 mM) before imaging. Live and dead cell viability assay was used for separately staining the samples. Briefly, propidiumiodide (PI) solution (2 µL, 1 mg/mL in DMSO) was added to each well followed by 15 min of incubation for staining dead cells, while the live cells without the QC samples were stained with the same

View Article Online
DOI: 10.1039/C7NR02229H

amount of calcein AM solution. Finally, each well was washed with PBS twice and then transferred for PL imaging.

3. Results and discussions

3.1. Synthesis and characterization of Au(en)QCs and Tf-Au(en)QCs.

We employed a simple phase transfer system to create water-soluble AuQCs from Bt-AuNPs in organic solvent. The phase transfer was induced in the presence of en, as both ligand replacement and stabilizing reagent, resulting in a water-immiscible QC with an Au-en coordination mimics an anticancer Au complex ($Au(en)Cl_2$). The QCs were encapsulated into the Tf, in the presence of Na_2CO_3, showing similar characteristics of fluorescence as presented in Au(en)QCs. Panels in **Fig. 1b** show the sample photos, exhibiting significant photoactivity upon a UV light.

Compared with a surface plasmon resonance (SPR) curve of Bt-AuNPs at 520 nm in the UV-vis absorbance spectrum, the AuQCs exhibited a dramatically blue-shifted absorption onset at 310 nm with a shoulder around 250 nm (**Fig. 2a**). Thus, it proposes that the host AuNPs found to be fragmented to a very small NCs as a characteristic of quantum-sized NC formation via NP-etching process.[19] The purification steps were effective for improving the uniformity of the QCs by discarding larger sized non-fluorescent NPs as byproducts. Rather than a flat characteristic shoulder peak of quantum sized NCs, the unique absorbance peak at 310 nm is noteworthy because it proposes that heterocyclic en ligands were formed on the AuNCs, whereas free en ligands do not possess aromatic rings that absorb in this band. Notably, absorption features of AuQCs are different from that of AuQCs embedded in apo-Tf proteins,

View Article Online
DOI: 10.1039/C7NR02229H

observing the onset of the curve was faded by which this absorption variation highlights successful incorporation of the QCs inside the metal binding pockets of apo-Tf proteins. The AuQCs and Tf-AuQCs maintain their high steady-state PL and narrow blue emission at 473 nm (**Fig. 2b**). The PL spectra of both AuQCs and Tf-AuQCs showed same intensity of excitation and emission curves at 318 nm and 473 nm, respectively (**Fig. S1**). The large Stokes shift in the emission where the absorption band shoulder appears at around 318 nm and the PL-emission maximum is shown at 473 nm, is correlated with the excited state, which is likely to have a significant geometric alteration. Apparently, their interfacing through a ligand replacement between thiol-ligands (Bt) on AuNPs and incoming excess amino-ligands (en) due to the affinity difference of these ligands on Au would result in a non-equilibrium coexistence system, which is responsible for releasing Au ions from AuNPs. Hence a conversion into a continuous size-trim downed UV responsive cluster dimension would be occurred so as to form an equilibrium state that may be consisted of a few atomic Au cores and monolayer of en-ligand-coordinating Au atoms, as similarly discussed in the report using poly-ethyleneimine (PEI).[19] This transition can be often observed where SPR from AuNPs diminishes and PL arises at the AuQC size regime, which is known that the PL property is attributed to molecule-like transitions due to their finite cluster size.[1-6] According to the spherical Jellium model,[6] smaller AuQCs emit stronger PL at shorter wavelengths. As a result of PL spectra versus a quinine standard (QY=53%), the photophysical property of AuQC and Tf-AuQC samples showed relatively high QYs of 26 ± 0.3 % and 24 ± 0.6 %, respectively, which is superior to that of previously studied etching-based AuQCs (QY=4~20%),[1-3, 18-21] as well as Au complex-based PL-

View Article Online
DOI: 10.1039/C7NR02229H

compounds (QY=10~15%).[33-36] Furthermore, both QC samples showed very good PL-stability, allowing to vaporize the water under vacuum and to re-disperse them again preserving intact their PL properties, while traditional organic dyes usually demonstrate fast photobleaching, and thus, enabling us to use for bio-labeling/imaging. High QY level of AuNCs is mainly associated with well-defined Au core size with its intrinsic quantization effects and the surface properties of which are directed by the chemical interfaces between the Au core and the surface ligands.[25] Usually, the synthetic method (either a reduction- or etching-based approach) involves the formation of non-fluorescent NPs as byproducts as well as inhomogeneous Au cores, which can lower the synthetic yield, purity, and PL QY level.[7] For example, Liu *et al* reported that dimethylformamide (DMF)-protected AuNCs,[37] which involved a mixture of various-sized AuNCs of less than 20 atoms including at least Au_8 and Au_{13}; the ssDNA-protected AuNCs[18] contain Au_7 (~0.9 nm) of Au^+ and Au^0 cores; PEI-etched Au_8NCs also contain larger AuNPs.[19] In this report, the increased QY level would be primarily attributed to the defined small Au_8 core size by excluding larger counterparts and other valenced Au cores, via the several purification steps that were efficient for improving the monodispersity and QY of the QCs. In addition, the unique surface such as heterocyclic en ligand-Au interface would also play a major role in the high QY of the QCs.

Recently, to gain fundamental insights into the origin of PL in AuQCs, Martinez *et al* recently synthesized ssDNA-templated luminescent Au_7QCs that the PL of QCs are attributed to the cationic Au^+ states, rather than Au^0 form in the presence of sulfur.[18] Whereas bigger sized AuNCs (>1 nm) with rigid ligands are mostly Au^0 state and their

View Article Online
DOI: 10.1039/C7NR02229H

PL properties are supposed to be independent to an additional reduction, the valenced states of subnanometer QCs against sulfurs are supposed to play a significant functional role in PL, as well as redox property.[18] Likewise, in our study, since the PL of AuQCs were lessened as GSH concentration increased (**Fig. S2a**), we attempted to protect the QCs by embedding into a surface-protective carrier, e.g., Tf, for the purpose of targeting cancer cells and avoiding undesirable cytotoxicity against normal cells. The loading efficiency was ~43.8% in the presence of sodium carbonate (20 mM) (**Fig. S2b**), in good agreement with the report that metal ion couples to apo-Tf only in the presence of carbonate that serves as a linker between cationic metals and proteins.[38] Remarkably, no significant effects in the loss of PL intensities were observed for the Tf-encapsulation of QCs (**Fig. 2b**), implying that the Tf-Au binding did not influence the PL property due to the weak interaction between Tf and Au, rather than covalent binding that triggers Au reduction or aggregation resulting in loss of PL.

Based on the high-resolution TEM result, the size of monodispersed Bt-AuNPs was ~2.5 nm (**Fig. 2c**), whilst the DLS analysis confirmed uniform distribution with hydrodynamic diameter of 3.08 ± 1.1 nm (**Fig. S3**). On the other hand, the mean diameter of AuQCs (>90 % conversion of Au atoms on NPs) was determined to be 0.87 ± 0.27 nm by the TEM size distribution analysis (**Fig. 2d, Fig. S4**). Typically, the atomic clusters smaller than 1 nm are too small to be visible under TEM observations. For example, the DMF-protected Au_{11} clusters are not visible under TEM.[37] As a rare case, the size of ssDNA-protected Au_7 clusters were barley determined to be ~0.9 nm,[18] which can support our TEM result. The Bt-AuNPs' substantial size reduction and

View Article Online
DOI: 10.1039/C7NR02229H

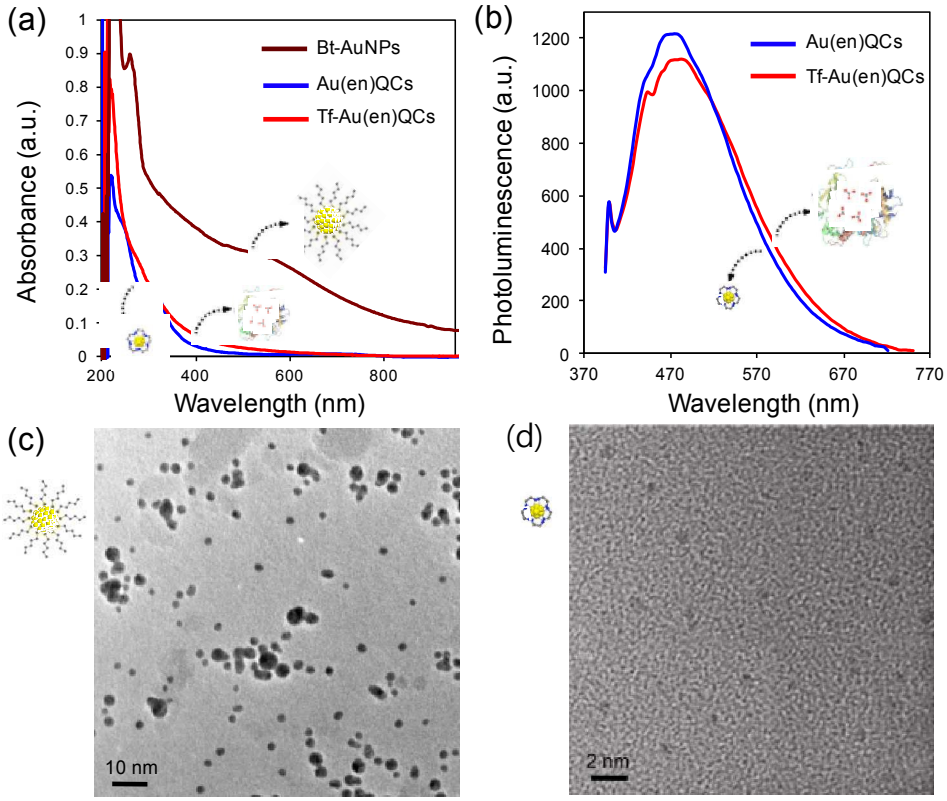

compositional changes were also proven by the energy-dispersive X-ray (EDX) spectra (**Fig. S5**). Thus, contrasting the hyperbranched-ligand (PEI) stabilized AuQCs,[19] these methodologies are the first successful top-down etching methods on AuNPs using the smallest ligands (e.g.,

Fig. 2 Optical and morphological characterizations. (a) UV-vis-absorbance and (b) PL spectra of Au(en)QCs and Tf-Au(en)QCs. (c) TEM of Bt-AuNPs, (d) HRTEM of Au(en)QCs.

en), which could produce more diminutive QCs than the conventional QCs in the final size with ligands.

View Article Online
DOI: 10.1039/C7NR02229H

The exact number of atoms present in the core of these NCs have been determined by a positive mode MALDI-TOF MS analysis (**Fig. 3a**). The monodispersed maximum mass was observed at ~2038.1 m/z with the interspacing of 1 m/z (**Fig. 3a**, inset), which reveals the AuQC was formulated as an 8-atom Au ligated by 8 en molecules (Au:N=1:2) with the oxidation state of +1. Based on the X-ray photoelectron spectra (XPS) (**Fig. 3b**). The principal Au core level spectrum of the QCs shows an intense and sharp peak at ~84.7 eV and a less intense peak at ~88.25 eV, corresponding to the Au $4f_{7/2}$ and Au $4f_{5/2}$, respectively, which reveals that the AuQC has characteristics of clusters with Au^{+} oxidation states, correlating to the MS result. The N 1s XPS spectrum (**Fig. 3b,** inset) also confirms that typical peak of NH_2 species from the en ligands at 401.3 eV was shifted to 398.7 eV, offering an insight into that N atoms of en are adsorbed on Au in the AuQC rather than remaining as NH_2. From these spectra, the relative atomic % of Au and N are found to be 0.82% and 1.6%, correspondingly, yielding Au-N with 1:2 ratio, which is also approved with the MS result. Therefore, the QCs are referred as $[Au_8(en)_8]^{+}$, mimicking a structural coordination of $Au^{+}(en)Cl_2$, which confirms our initial rationale that the en-ligand is critical in forming the anticancer-active charged Au moiety and protecting the QCs.

3.2. Simulation of Au(en)QCs

With the help of MALDI-TOF-MS and XPS results on AuQC structure, to predict the precise structure of AuQCs, we have conducted First principle calculations, revealing that a theoretical structure of QC is a cube with symmetry of P_1. Markedly, in the presence of en ligands on the NCs, the structure at the lowest energy evolved to form a

View Article Online
DOI: 10.1039/C7NR02229H

rhombohedral cube with a chiral symmetry of C_1 (**Fig. 3c, i** and **Movie S1**). The shape of QC isomer is equivalent with the excited state with large Stokes shift due to its distorted cubic structure, which is clearly distinctive comparing previously reported models of Au_8 isomers that typically exhibit a group of nonplanar nugget shape (T_d, C_{2v}, D_{2d}) at the lowest energy.[39] Comparing with the structure of Au_n (n>8) QCs that have been relatively resolved, the studies on revealing Au_n (n<9) QC structure have been challenged because the prediction of ligand effects on the Au structure formation is difficult.[39] Based on our geometric and electronic structure calculations of bonding energies of the en-ligated AuQCs, it holds potentially high chemical stability in the bonds between their Au_8 kernels and the en rings, where the two N-groups of en rings were tightly attached on each gold atom, enabling rigid covalent binding of Au-N. Accordingly, the QCs showed isosurfaces of electrophilic (**Fig. 3c, ii**) and nucleophilic (**Fig. 3c, iii**), denoting that the AuQCs can be chemo-sensitive against reactive counter molecules, whilst no radical entity was found in the QCs. The HOMO-LUMO gap of the cluster was found to be 0.1456 eV, greatly lower than that of the Au_8 nuggets (1.2874-1.8882 eV),[39] presuming that our QCs are chemically reactive most likely due to the amphoteric (redox) charge characteristic of Au^+-en-coordination, rather than a neutral Au structure, in consisted with the CV, gel electrophoresis, and the biological activity results as descried in the next section. In other words, the small E gap might be attributed to the covalent link between the electron donor of en ligand (high HOMO) and electron acceptor of Au^+ (low LUMO) in the Au-N coordination, as discussed in the literature.[40] Besides, the powder X-ray diffraction (XRD) pattern of AuQCs (**Fig. S6**) showed that a single crystal feature with air scattering, which is analogous to the

View Article Online
DOI: 10.1039/C7NR02229H

previous results on aggregated Au complex-based fluorescence AuNCs,[33-36] unlike that of common AuNCs. Thus, this result supports that our product possesses a structural novelty over

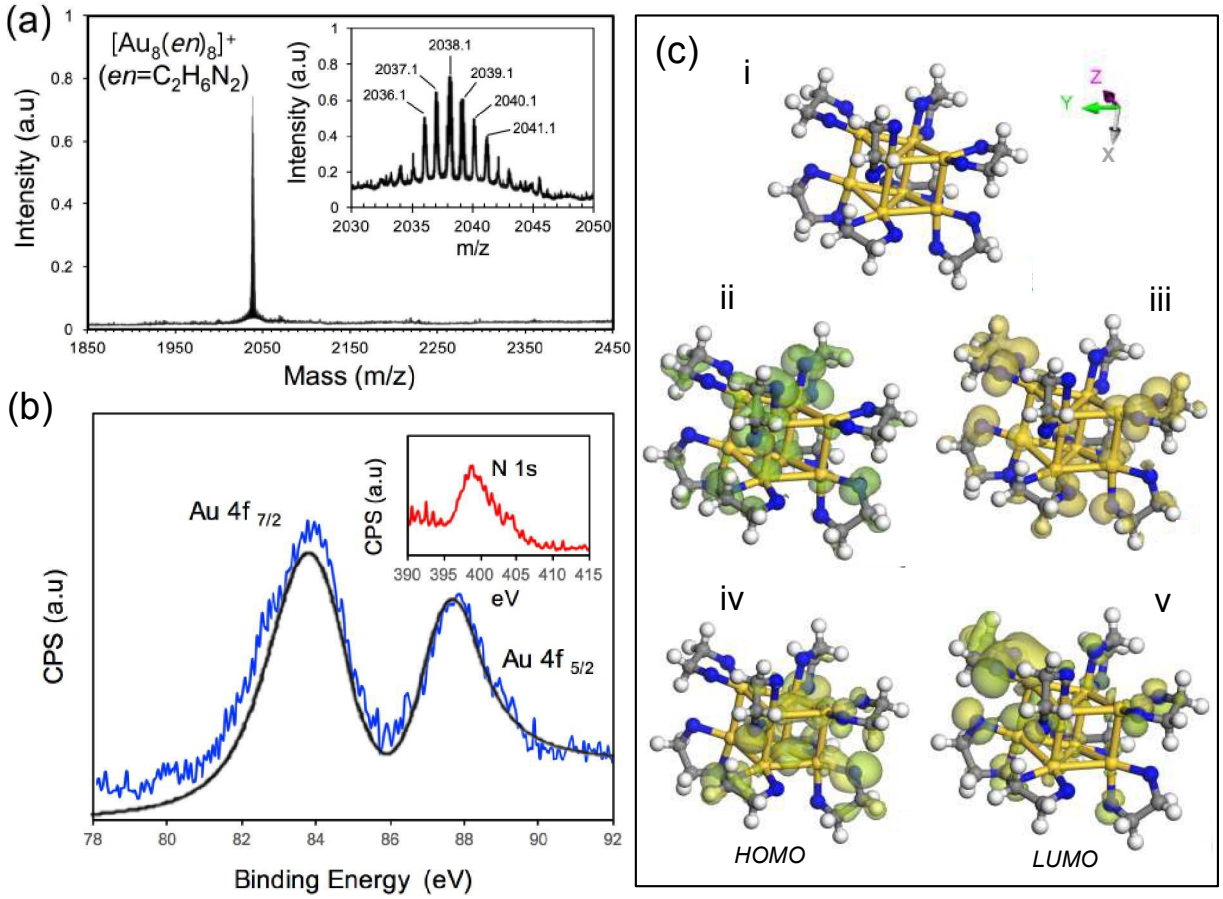

Fig. 3 Structural characterizations of Au(en)QCs. (a) MALDI-TOF mass spectrum (inset: an isotopic spectrum) of Au(en)QC. (b) Au 4f core level photoelectron spectrum of the Au(en)QCs (inset: N 1s core level photoelectron spectrum of the QCs). (c) The simulated Au(en)QC structures. The 3-D structure of Au_8 cluster with en rings (i) and its electrophilic (ii), nucleophilic (iii), HOMO (iv), and LUMO (v) states.

View Article Online
DOI: 10.1039/C7NR02229H

traditional AuNCs. In view of our early hypothesis that our QCs imitate a clustered Au^{+}(en) complex, the Au(en) moiety at the confined size-transition aggregates into a QC, becoming emissive due to intermolecular aurophilic interactions,[33-36] which can be allocated to the weak intermolecular Au···Au interaction between the closest pair of Au atoms,[33] aside from the shortened Au···Au contacts via the thermodynamic stabilization.[36]

3.3. Fluorescence imaging and therapeutic activity of Au(en)QCs

To evaluate *in vitro* efficacy of the AuQCs in cellular uptake and labeling, we performed a confocal fluorescence imaging. The QCs were transported into cells and located in the cytoplasm, fluorescing blue color (**Fig. 4a**). The bright PL intensity indicates that outstanding cellular uptake due to their small size. However, the cell morphology was found to be changed over time, representing that they were dead after 24 h incubation with the QCs (**Fig. 4b**), which also confirmed by a dead cell imaging in **Fig. S7a**. In the presence of possible physiological interference, BSA, the medium sample containing 20 mM BSA with the QCs at pH 7.0 showed substantial toxicity, except at pH 12 where the reduction ability of BSA activated the thiol-Au bonding on the QCs, resulted in inert.

Likewise, the QC sample containing 20 mM GSH showed substantially decreased cell death as a consequence of the high thiol reactivity of Au^{+} in the QCs, resulted in low cytotoxicity (**Fig. S7b**), reflecting that such a standalone AuQC structure is reactive to thiols, in accordance with the results of PL of AuQCs under GSH (**Fig. S2a**) and the simulation-based chemical reactivity (**Fig. 3c, ii, iii**).

View Article Online
DOI: 10.1039/C7NR02229H

Fig. 4 Confocal microscopic images of ovarian cancer cells (A2780) after incubation with Au(en)QCs (20 μM) for (a) 2 h and (b) 24 h. (i) Merged bright field (BF) and DAPI, (ii) magnified BF, and (iii) DAPI modes, demonstrating morphological change of cells. Scale bar: 40 μm.

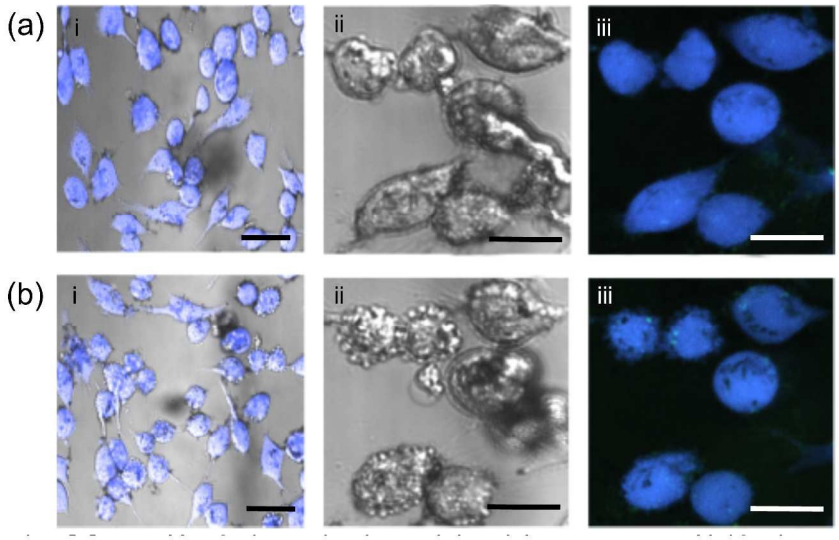

Fig. 4 Confocal microscopic images of ovarian cancer cells (A2780) after incubation with Au(en)QCs (20 μM) for (a) 2 h and (b) 24 h. (i) Merged bright field (BF) and DAPI, (ii) magnified BF, and (iii) DAPI modes, demonstrating morphological change of cells. Scale bar: 40 μm.

3.4. Structural and physico-chemical characterizations of Tf-Au(en)QCs.

The TEM and AFM results exhibited the size of a Tf-encapsulated AuQC is ~5 nm and ~5.6 nm, correspondingly (**Fig. 5a,b**), while the hydrodynamic size via a DLS analysis was ~20.3 nm (**Fig. S8a**). The MALDI-TOF analysis showed a distinct peak at 81025 and a slight peak at 329985 m/z (**Fig. 5c**), pointing out dissociated Tf proteins and a

View Article Online
DOI: 10.1039/C7NR02229H

trace of some non-dissociated Tf-AuQC complexes, correspondingly. The first curve at ~81k m/z is identical with that of free apo-Tf (~81k Da) (**Fig 5c**, inset), which indicates that the AuQCs and Tf were dissociated because they are not covalently bound in good agreement with the PL stability. On the other hand, the AuQCs and functional groups of Tf proteins (e.g., thiols of cysteine) can be non-specifically adsorbed by the UV laser light (337 nm) of MALDI, and some of the adsorbed ones were appeared in the second peak at ~330k m/z in the MS spectrum: the use of the MS soft ionization process allows us to postulate the mass of Tf-AuQCs can be detectable in the MALDI-MS as an alternative means of tracking weakly bound metal-protein complex samples. All these data implied that ~10 QCs (core) may be loaded into 4~5 Tf molecules (~5 nm shell), leading to a ~20 nm core-shell drug delivery formulation as simulated in **Fig. 1a**. Besides, to verify electrochemical feature of the Tf-AuQCs over the free AuQCs, cyclic voltammetry (CV) was performed. The CV data of the AuQCs (**Fig. 5d**) showed two closely adherent peak currents at 0.083 and 0.188 V in related to a sequential one-electron oxidation/reduction (double Au^{+}/Au^{0} processes) of the QCs,[18] whereas observed disappearance of the peak currents in Tf-AuQC sample is characteristic of the formation of core-shell nanostructure. In addition, the 2% agarose gel electrophoretic migration pattern of the QC products determined not only their surface charge characteristics, but also outstanding photostability over the continuous electric field, along with high monodispersity and purity in water (**Fig. 5e**). Likewise, the zeta potential analyses of the AuQCs and Tf-AuQCs showed +26.5 mV and -27.3 mV, respectively, confirming the outstanding colloidal stability and charge property **(Fig. S8b)**. Furthermore, the AuQCs exhibited high photostability at all pHs (4~8) without showing

View Article Online
DOI: 10.1039/C7NR02229H

any substantial aggregation or reduced PL under ambient condition for at least 6 months, except a prolonged exposure at pH 2-3 and pH 9-10 led to slight decrease in the PL intensity (**Fig. S9a**). The extraordinary stability was probably due to the tightly ligated bifunctional amine ligands of the en on each Au atom of AuQCs. During the etching

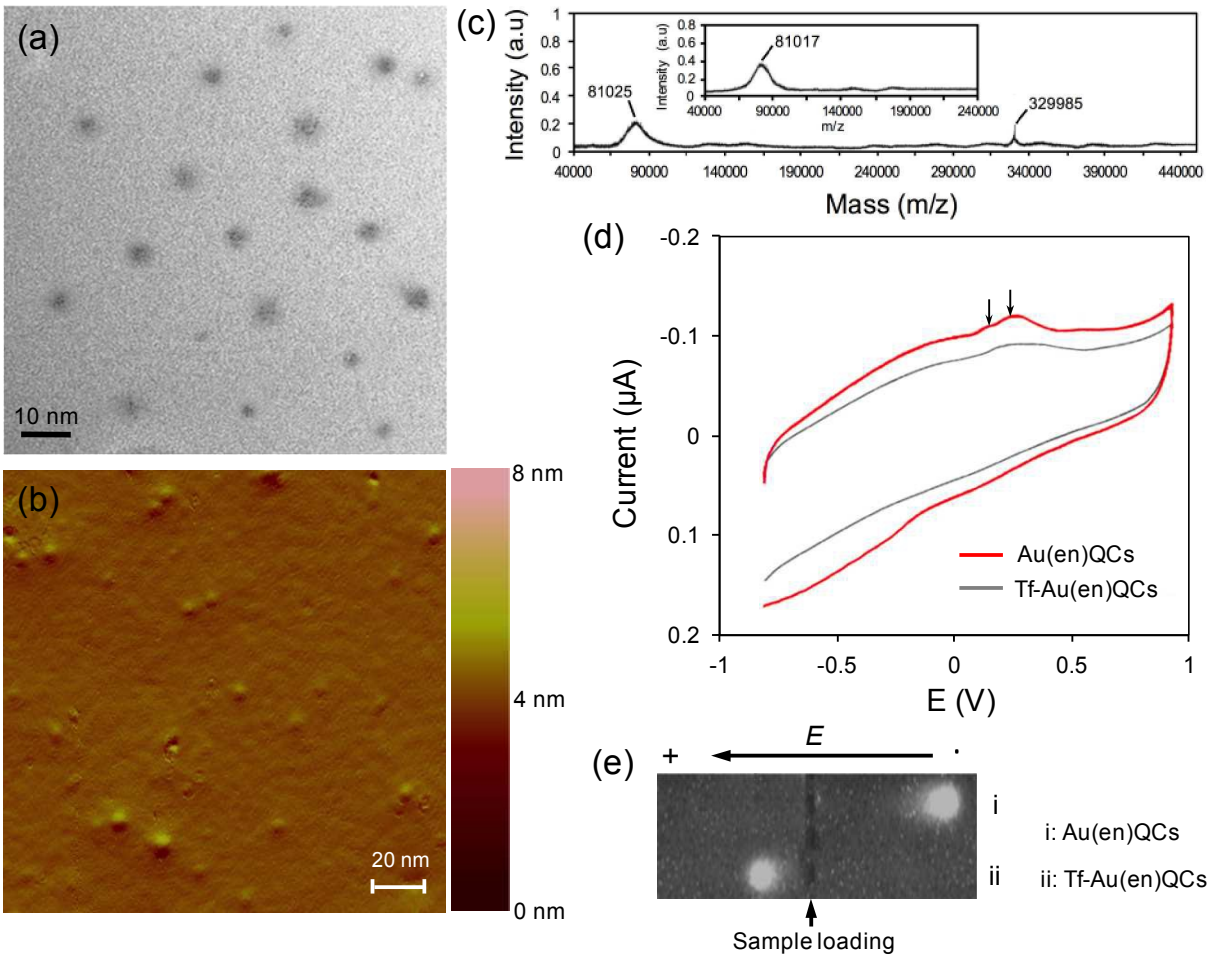

Fig. 5 Structural analysis of Tf-Au(en)QCs using (a) TEM, (b) AFM, and (c) MALDI-TOF MS (inset: a control MS of free Tf). Surface characteristics of Tf-Au(en)QCs by (d) cyclic voltammetry in contrast to Au(en)QCs and (e) the gel electrophoretic analysis (the

View Article Online
DOI: 10.1039/C7NR02229H

arrow: an electric field (E) applied to a gel matrix), verifying charge property and chemical purity.

process, these shell molecules are presumably packed on the surfaces of the AuNCs and shield them from direct contact with the solution. Comparing with Au(en)Cl_2 complexes that are known to undergo hydrolysis in water at pH >2.5~3.0,[30] the AuQCs are more thermally stable than Au(en)Cl_2 due to the replacement of 2 Cl ligands by adjacent gold atoms, allowing the QCs highly tolerant to oxidation over the broader pH range; the compact Tf-shells thoroughly encapsulate the core AuNCs, enabling appropriate optical stability at pH 7-8, except showing reduced PL which may be due to the dissociation/decomposition between the QCs and Tf proteins. These results allow us to propose that the AuQCs can be a promising potential as a powerful biotag-based assay tool. Based on the pH-dependent release study of the AuQCs, the QCs were released upto ~44.5% at pH 5.5 (**Fig. S9b**), which implies the release profile is associated with a pH-dependent metal-Tf binding kinetics, although the dissociation constant (K_d) of monovalent Tf would be lower than those of other complexes, e.g., Au^{3+}-Tf, Fe^{3+}-Tf, or Fe^{+}-Tf.[38,41] Furthermore, we performed that an electrophoretic analysis of the Tf-Au(en)QC samples at different biological pH, which also presented the dissociation of Au(en)QCs from the Tf-Au(en)QC complexes at pH 5.5 (**Fig. S10**). Hence, in a lysosomal condition at pH 5.5, the QCs were released in response to the pH, which supports the reversible interaction of the QCs inside Tf in the presence of the carbonate anions.

View Article Online
DOI: 10.1039/C7NR02229H

We also systematically investigated other effects such as salt concentrations of the solutions (0-0.5 M) and photo-irradiation (0-48 h) on the colloidal stability of the QCs. By kinetically monitoring the QY values with the PL-spectroscopy (**Fig. S11**), we found that the QCs are stable for quite a long time against an UV-irradiation (at least up to 18 h) in the presence of salt (up to 0.25 M), which was not induced evident quenching within possible intense environments, except an extreme condition at 0.25-0.5 M salts for 18-48 h exposure.

3.5. Anticancer imaging and targeting activity of Tf-Au(en)QCs.

Consequently, we employed the Tf-AuQC formulation as a nanocarrier design in order to evade the extracellular interferences and to improve targeting efficiency in a selective manner (because the AuQCs have relatively low selectivity between cancer cells and normal cells). Tf-encapsulation of the AuQCs to form Tf-AuQCs significantly improved both labeling efficiency and cytotoxicity to cancer cells (**Fig. 6a**), while showing minor cytotoxicity to normal ovarian cells (**Fig. 6b**). As presented in **Fig. 6c**, most of cancer cells were brightly labeled after 24 h incubation with the Tf-AuQCs (20 μM), and considerably dead (~66%), while only ~4% of the normal cells were nearly unlabeled and vaguely dead. This implies that the presence of surface Tf proteins on the AuQCs could inhibit a thiolate adsorption and prolong the drug circulation time *in vitro*. Release of the cargo into cytoplasm might be occurred due to the dissociation of the QCs from Tf shells in ribozyme pH (pH<7), leading to targeting and fluorescence staining, simultaneously. The mechanistic anticancer effect behind the release machinery can be presumed as illustrated in **Fig. 6d**: (i) When Tf-proteins are binding to their receptors on

View Article Online
DOI: 10.1039/C7NR02229H

the cell surface, (ii) the Tf-receptor complexes are promptly internalized and forms endosomes, where the complex is subjected to a drop in endosomal pH (pH 5.5-6.0), which weakens the linkage between Au^{+} and Tf: metal release from Tf normally involves protonation of the carbonate anion, relaxing the metal-protein bond.[38,41] The escaped QCs are ultrasmall enough to be penetrated in organelles, e.g., lysosomes, mitochondria, and nuclei, leading to antitumor targeting by cell necrosis or apoptosis. An excess amount of free-Tf sample against the tumor cells did not show any substantial toxicity, verifying the Tf-receptor-mediated tumor targeting efficacy of Tf-AuQCs (**Fig. S12**). As a result, *as*-synthesized QCs can be thought of as a "silent marker" of where the luminous anticancer marker is cloaked by metal transfer proteins against serum interferences, and executed the target only.

However, little is identified regarding the detail mechanistic cytotoxicity of AuNCs after they enter the cell organelles. In this study, we have found that the Au(en)QCs have high reactivity of their gold-ligand interface with large surface area-to-volume ratio that might be responsible for the generation of reactive oxygen species (ROS). Based on the bright color throughout the entire cell, it is certain that their ultrasmall size expedites their internalization into most of the cytoplasmic organelles, i.e., lysosomes, mitochondria, as well as cell nucleus through nuclear pores. Although the cell uptake efficiency is high, it is difficult to selectively localize the QCs in a specific organelle as described elsewhere.[42] Because most of the cell constituents including nucleus and mitochondria stained by the QCs, a possible mechanism for the cytotoxicity in the subcellular targeting can be proposed as follows: the QCs locate into nucleus and mitochondria induce ROS), causing cellular apoptosis via a mitochondrial damage

View Article Online
DOI: 10.1039/C7NR02229H

pathway. Therefore, further work is required to direct a better understanding of the toxicity mechanism of the QCs by examining the cellular parameters, such as cell signaling process, ROS level, and mitochondrial membrane potential, in addition to a site-specific trafficking and targeting of an organelle for advanced applications.

Most clinical anticancer agents are ineffective against drug-resistant cancers such as melanoma, non-small cell lung cancer, and glioblastoma,[43-45] since the drugs act through the induction of apoptotic cell death.[46,47] Recently, several metallodrugs have been explored as potential apoptosis-independent anticancer drug candidates.[48-51] In our study, contrasting conventional anticancer metal complexes, e.g., cisplatin and $Au(en)Cl_2$,

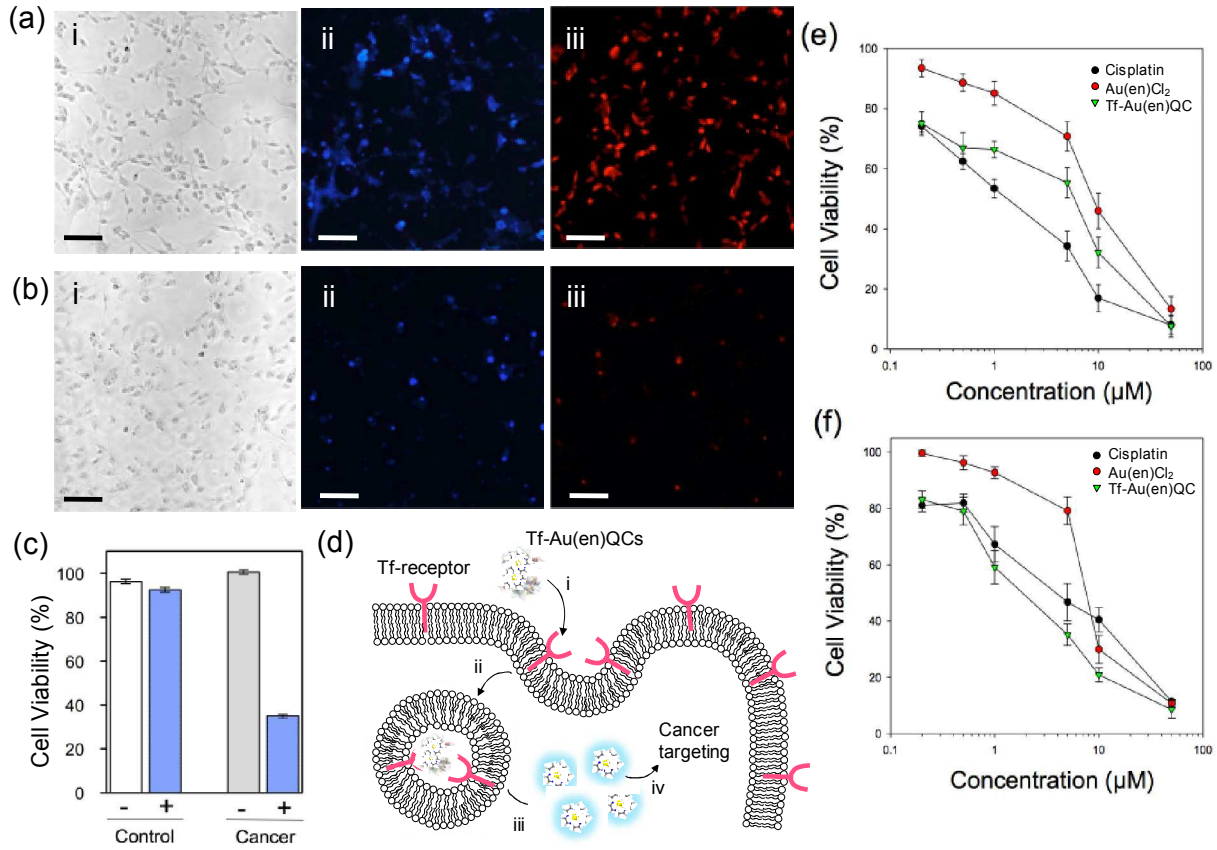

View Article Online
DOI: 10.1039/C7NR02229H

Fig. 6 Cancer cell imaging and targeting by Tf-Au(en)QCs. Microscopic images of (a) ovarian carcinoma (A2780) and (b) epithelial normal cells (SV40) stained with the 20 μM QCs, showing bright field (i), QC-labeled (ii), and dead (iii) cells. Scale: 200 μm. The corresponding cell viability by the XTT assay (c). Mechanism of Tf-receptor-mediated intracellular labeling of QCs and cancer treatment (d) by cell uptake via Tf-receptors (i), endocytosis (ii), and release into cytoplasm, where DNA in nuclei or mitochondria can be targeted, resulting in apoptosis/necrosis (iii). The dose-dependent cell proliferation profiles of the QCs over cisplatin-sensitive cells (A2780) (e) and cisplatin-resistant cells (A2780 *cis*) (f).

as-prepared Tf-AuQCs displayed the intrinsic cytotoxicity (EC50=~6 μM) that was substantially lower than that of cisplatin (EC50=~1.5 μM) against A2780 (cisplatin-sensitive) cells (**Fig. 6e**). Furthermore, they appeared to be much better cytotoxic in A2780 *cis* (cisplatin-resistant) cells (EC50=~2 μM) over A2780 (**Fig. 6f**), supporting our hypothesis described earlier about the different antitumor mechanism of action in contrast to that of cisplatin in which DNA is the only target: we can conclude that their cytotoxicity might be primarily derived from an alteration of mitochondrial function and inhibition of protein synthesis, along with the possible DNA damage. Therefore, this result would allow us to utilize as-prepared QC products for potential cancer targeting not only in sensitive and selective treatments, but in minimizing drug resistance and possible side effects.

Additionally, the QCs and Tf-AuQCs presented similar bioactivity against other cancer cell lines including HeLa and human melanoma cells (**Fig. S13**), which

View Article Online
DOI: 10.1039/C7NR02229H

envisages clinical efficacy for maximizing anticancer effects toward various tumors, as well as potentiating treatment for apoptosis-resistant cancers, e.g., melanoma. Although adding same quantity of AuQCs and Tf-AuQCs into the cell lines, the Tf-free distribution of AuQCs was appeared to be slightly more cytotoxic than the receptor-based pathway of Tf-AuQCs (**Fig. S13**), which might be due to a limited capacity of the Tf-receptors, where only 20% of them are on the cell surface in cancer cells,[52] e.g., HeLa cells, while the smaller sized AuQCs could be directly internalized through the cell membrane pores by passing the ligand-receptor recognition.

However, the ultrasmall size of AuNCs exhibited cytotoxicity as an immense concern based on several studies have informed their adverse effects.[51,53,54] In particular, the occurrence of drug/apoptosis resistance leads to the failure of tumor treatment, involving serious side effects, which is a challenging obstacle to overcome. A low selective anticancer drug with high drug resistance would require a higher concentration and continuous dose, inherently cause the side effects. Thus, the results in this report showed anticancer activity of as-prepared QC products for potential cancer targeting in sensitive and selective treatments, which minimized drug resistance or apoptosis-resistance with a single treatment in a low dose level. Accordingly, we believe that as-prepared QCs at least could minimize the overdose-provoked potential side effects. Nonetheless, we are unable to specify the detail side effects in this scope of investigation, because we have no *in vivo* results, e.g., inflammation, infection, or organ damage, to verify resolved biological response.

4. Conclusions

View Article Online
DOI: 10.1039/C7NR02229H

Novel Au(en)QCs were readily prepared by etching host AuNPs via a small-ligand (en)-exchange-assisted atomic clustering technique. The physico-chemical studies of the QCs disclosed that its atomically precise unique structure is a subnanometer-sized rhombohedral cubic Au cluster, which composed with eight of Au atoms and en ligands, holding eight anticancer motifs of Au^{+}(en) complex in a single super-atomic system. Extraordinarily, they exhibited highly bright and stable blue PL with high QY, good water-solubility, electrochemical redox-activity, and anticancer activity. Moreover, the anticancer QC-delivery vehicles were formulated by encapsulating the QCs in apo-Tf proteins via weak Au-Tf affinity, presenting enhanced cancer targeting efficacy in high capacity loading, cancer-selective imaging, controlled release, and cancer-specific targeting (especially effective for drug-resistant tumors). These novel QC-protein hybrids would be appropriate multipurpose biotags for intracellular imaging/targeting as an alternative metal complex-based chemotherapeutic drug, due to their ultrafine size, robust photostability, and selective anticancer activity. Even if the Tf-Au(en)QCs showed early signs of multifunctional minimally-invasive biocompatible drug delivery carrier, it is expected that many more *in vivo* and *in vitro* trials will be piloted toward generic theranostic clinics beyond the current research stage. Yet, further mechanistic optical investigation of the missing link between the super-atomic scale (Au_8 core) and molecular scale that is associated with the PL property of ligand-Au clusters, together with further biological effects of the Au(en)QCs, remains to be explored.

Electronic supplementary information (ESI) Available: The ESI is available free of charge on the RSC Publications website at DOI:

View Article Online
DOI: 10.1039/C7NR02229H

A movie file of Au(en)QC simulation (**Movie S1**); The additional figures as described in the text (**Fig S1-S13**).

Acknowledgement. The authors thank Mr. Toshio Sasaki (OIST-Graduate University, Japan) for the technical support for TEM imaging; and Dr. Jin-Woo Kim (University of Arkansas at Fayetteville, US) for the valuable comments.

References

1. T. Tsukuda and H. Häkkinen, Protected metal clusters: from fundamentals to applications, Elsevier, 2015.
2. R. Jin, C. Zeng, M. Zhou, and Y. Chen, *Chem. Rev*. 2016, **116**, 10346-10413.
3. R. Jin, *Nanoscale* 2015, **7**, 1549-1565.
4. R. Jin, Y. Zhu, and H. Qian, *Chem.-Eur. J*. 2011, **17**, 6584-6593.
5. J. F. Parker, C. A. Fields-Zinna, R. W. Murray, *Acc. Chem. Res*. 2010, **43**, 1289-1296.
6. J. Zheng, P. R. Nicovich, and R. M. Dickson, *Ann. Rev. Phys. Chem*. 2007, **58**, 409-431.
7. S. Palmal, and N. R. Jana, *Wiley Interdiscip. Rev. Nanomed. Nanobiotechnol*. 2014, **6**, 102-110.
8. C. Zhou, S. Yang, J. Liu, M. Yu, and J. Zheng, *Exp. Biol. Med.* 2013**, 238**, 1199-1209.
9. L. Shang, S. Dong, and G. U. Nienhaus, *Nano Today* 2011, **6**, 401-418.
10. L. Zhang, E. Wang, *Nano Today*, 2014, **9**, 132-157.

View Article Online
DOI: 10.1039/C7NR02229H

11. L.-Y. Chen, C.-W. Wang, Z. Yuan, and H.-T. Chang, *Anal. Chem.* 2015, **87**, 216-229.
12. X. Qu, Y. Li, L. Li, Y. Wang, J. Liang, and J. Liang, *J. Nanomater*. 2015, **2015**, 784097.
13. C. Ding, and Y. Tian, *Biosens. Bioelectron.* 2015, **65**, 183-190.
14. H.-C. Chang, Y.-F, Chang, N.-C. Fan, and J. A. Ho, *ACS Appl. Mater. Inter.* 2014, **6**, 18824-18831.
15. D. Tian, Z. Qian, Y. Xia, and C. Zhu, *Langmuir*, 2012, **28**, 3945-3951.
16. J. Liu, K. S. Krishna, Y. B. Losovyj, S. Chattopadhyay, N. Lozova, J. T. Miller, J. J. Spivey, and C. S. Kumar, *Chemistry* 2013, **19**, 10201-10208.
17. G. Li, and R. Jin, *Acc. Chem. Res*. 2013, **46**, 1749-1758.
18. S. Chakraborty, S. Babanova, R. C. Rocha, A. Desireddy, K. Artyushkova, A. E. Boncella, P. Atanassov, and J. S. Martinez, *J. Am. Chem. Soc*. 2015, **137**, 11678-11687.
19. H. Duan, and S. Nie, *J. Am. Chem. Soc.* 2007, **129**, 2412-2413.
20. R. Zhou, M. Shi, X. Chen, M. Wang, H. Chen, *Chem-Eur J.* 2009, **15**, 4944-4951.
21. T. A. Dreier, and C. J. Ackerson, *Angew. Chem. Int. Ed.* 2015, **54**, 9249-9252.
22. N. Goswami, Q. Yao, Z. Luo, J. Li, T. Chen, and J. Xie, *J. Phys. Chem. Lett.*, 2016, **7**, 962-975.
23. Y. Kamei, Y. Shichibu, and K. Konishi, *Angew. Chem. Int. Ed*. 2011, **50**, 7442-7445.
24. W. W. Xu, B. Zhu, X. C. Zeng, and Y. A. Gao, *Nat. Commun*. 2016, **7**, 13574.
25. Z. Wu, and R. Jin, *Nano Lett*. 2010, **10**, 2568-2573.
26. I. Romero-Canelon and P. J. Sadler, *Inorg. Chem*. 2013, **52**, 12276-12291.

View Article Online
DOI: 10.1039/C7NR02229H

27. T. Zou, C. T. Lum, C.-N. Lok, J.-J. Zhang, and C.-M. Che, *Chem. Soc. Rev*. 2015, **44**, 8786-8801.

28. I. Ott, and R. Gust, *Arch. Pharm. Chem. Life Sci.* 2007, **340**,117-126.

29. M. J. Hostetler, J. E. Wingate, C.-J. Zhong, J. E. Harris, R. W. Vachet, M. R. Clark, J. D. Londono, S. J. Green, J. J. Stokes, G. D. Wignall, G. L. Glish, M. D. Porter, N. D. Evans, R. W. Murray, *Langmuir* 1998, **24**, 17-30.

30. S. Zhu, W. Gorski, D. R. Powell, and J. A. Walmsley, *Inorg. Chem.* 2006, **45**, 2688-2694.

31. B. Delley, *J. Chem. Phys*. 1990, **92**, 508-517.

32. B. Delley, *J. Chem. Phys*. 2000, **113**, 7756-7764.

33. R. L. White-Morris, M. M. Olmstead, S. Attar, and A. L. Balch, *Inorg. Chem.* 2005, **44**, 5021-5029.

34. R. Gavara, J. Llorca, J. C. Lima, and L. A. Rodriguez, *Chem. Commun.* 2013, **49**, 72-74.

35. M. Baron, C. Tubaro, A. Biffis, M. Basato, C. Graiff, A. Poater, A. Cavallo, N. Armaroli, and G. Accorsi, *Inorg. Chem.* 2012, **51**,1778-1784.

36. N. L. Coker, J. A. Krause Bauer, and R. C. Elder, *J. Am. Chem. Soc*. 2004, **126**, 12-13.

37. X. Liu, C. Li, J. Xu, J. Lv, M. Zhu, Y. Guo, S. Cui, H. Liu., S. Wang, Y. Li, *J. Phys. Chem. C* 2008, **112**, 10778-10783.

38. M. S. Shongwe, C. A. Smith, E. W. Ainscough, H. M. Baker, and E. N. Baker, *Biochemistry* 1992, **31**, 4451-4458.

39. S. A. Serapian, M. J. Bearparka, and F. Bresme, *Nanoscale*, 2013, **5**, 6445-6457.

View Article Online
DOI: 10.1039/C7NR02229H

40. D. F. Perepichka and M. R. Bryce, *Angew. Chem. Int. Ed*. 2005, **44**, 5370-5373.

41. H. V. Aposhian, R. M. Maiorino, D. Gonzalez-Ramirez, M. Zuniga-Charles, Z. Xu, K. M. Hurlbut, P. Junco-Munoz, R. C. Dart, and M. M. Aposhian, *Toxicology* 1995, **97**, 23-38.

42. J.-Y. Zhao, R. Cui, Z.-L. Zhang, M. Zhang, Z.-X. Xie and D.-W. Pang, *Nanoscale*, 2014, **6**, 13126-13134.

43. M. S. Soengas and S. W. Lowe, *Oncogene* 2003, **22**, 3138-3151.

44. I. Paul and J. M. Jones, *World J. Clin. Oncol*. 2014, **5**, 588-594.

45. C. Krakstad and M. Chekenya, *Mol. Cancer* 2010, **9**, 135.

46. U. Fischer and K. Schulze-Osthoff, *Cell Death Differ*. 2005, **12**, 942-961.

47. D. Wang and S. J. Lippard, *Nat. Rev. Drug Discovery*, 2005, **4**, 307-320.

48. S. Tian, F. M. Siu, S. C. Kui, C. N. Lok and C. M. Che, *Chem. Commun*. 2011, **47**, 9318-9320.

49. J. J. Soldevila-Barreda, I. Romero-Canelon, A. Habtemariam and P. J. Sadler, *Nat. Commun*. 2015, **6**, 6582.

50. M. J. Chow, C. Licona, G. Pastorin, G. Mellitzer, W. H. Ang and C. Gaiddon, *Chem. Sci.*, 2016, **7**, 4117-4124.

51. M. J. Chow, M. Alfiean, G. Pastorin, C. Gaiddone, and W. H. Ang, *Chem. Sci.* 2017, DOI: 10.1039/C7SC00497D.

52. J. E. Lamb, F. Ray, J. H. Ward, J. P. Kushner, and J. Kaplan, *J. Biol. Chem*. 1983, **258**, 8751-8758.

53. Y. Pan, S. Neuss, A. Leifert, M. Fischler, F. Wen, U. Simon, G. Schmid, W. Brandau and W. Jahnen-Dechent, *Small*, 2007, **3**, 1941-1949.

View Article Online
DOI: 10.1039/C7NR02229H

54. X. D. Zhang, D. Wu, X. Shen, P. X. Liu, F. Y. Fan and S. J. Fan, *Biomaterials*, 2012, **33**, 4628-4638.